

# Light-induced giant enhancement of nonreciprocal transport at KTaO<sub>3</sub>-based interfaces

Xu Zhang<sup>1,†</sup>, Tongshuai Zhu<sup>2,3,†</sup>, Shuai Zhang<sup>2,†</sup>, Zhongqiang Chen<sup>1</sup>, Anke Song<sup>1</sup>,  
Chong Zhang<sup>1</sup>, Rongzheng Gao<sup>1</sup>, Wei Niu<sup>1</sup>, Yequan Chen<sup>1</sup>, Fucong Fei<sup>2</sup>, Yilin Tai<sup>4</sup>,  
Guoan Li<sup>5</sup>, Binghui Ge<sup>4</sup>, Wenkai Lou<sup>6</sup>, Jie Shen<sup>5</sup>, Haijun Zhang<sup>2</sup>, Kai Chang<sup>6</sup>,  
Fengqi Song<sup>2,\*</sup>, Rong Zhang<sup>1,7,\*</sup> & Xuefeng Wang<sup>1,\*</sup>

<sup>1</sup>Jiangsu Provincial Key Laboratory of Advanced Photonic and Electronic Materials, State Key Laboratory of Spintronics Devices and Technologies, School of Electronic Science and Engineering, Collaborative Innovation Center of Advanced Microstructures, Nanjing University, Nanjing 210093, China

<sup>2</sup>National Laboratory of Solid State Microstructures, School of Physics, Nanjing University, Nanjing 210093, China

<sup>3</sup>College of Science, China University of Petroleum (East China), Qingdao 266580, China

<sup>4</sup>Information Materials and Intelligent Sensing Laboratory of Anhui Province, Institutes of Physical Science and Information Technology, Anhui University, Hefei 230601, China

<sup>5</sup>Beijing National Laboratory for Condensed Matter Physics and Institute of Physics, Chinese Academy of Sciences, Beijing 100190, China

<sup>6</sup>State Key Laboratory for Superlattices and Microstructures, Institute of Semiconductors, Chinese Academy of Sciences, Beijing 100083, China

<sup>7</sup>Department of Physics, Xiamen University, Xiamen 361005, China

<sup>†</sup>These authors contributed equally: Xu Zhang, Tongshuai Zhu, Shuai Zhang

**\*E-mail:** songfengqi@nju.edu.cn; rzhang@nju.edu.cn; xfwang@nju.edu.cn

**Nonlinear transport is a unique functionality of noncentrosymmetric systems, which reflects profound physics, such as spin-orbit interaction, superconductivity and band geometry. However, it remains highly challenging to enhance the nonreciprocal transport for promising rectification devices. Here, we observe a light-induced giant enhancement of nonreciprocal transport at the superconducting and epitaxial  $\text{CaZrO}_3/\text{KTaO}_3$  (111) interfaces. The nonreciprocal transport coefficient undergoes a giant increase with three orders of magnitude up to  $10^5 \text{ A}^{-1}\text{T}^{-1}$ . Furthermore, a strong Rashba spin-orbit coupling effective field of 14.7 T is achieved with abundant high-mobility photocarriers under ultraviolet illumination, which accounts for the giant enhancement of nonreciprocal transport coefficient. Our first-principles calculations further disclose the stronger Rashba spin-orbit coupling strength and the longer relaxation time in the photocarrier excitation process, bridging the light-property quantitative relationship. Our work provides an alternative pathway to boost nonreciprocal transport in noncentrosymmetric systems and facilitates the promising applications in opto-rectification devices and spin-orbitronic devices.**

## Introduction

Recently, nonlinear transport has been regarded as a sophisticated probe of the symmetry breaking in non-centrosymmetric materials/heterostructures<sup>1</sup>. Inversion symmetry breaking changes the original electronic band structure, thus generating a myriad of intriguing physical properties, such as nonlinear Hall effect<sup>2</sup>, quantum metric dipole<sup>3,4</sup>, bulk photovoltaic effect<sup>5</sup>, circular photogalvanic effect<sup>6</sup>, and helicity dependent terahertz emission<sup>7</sup>. Another striking example is the nonreciprocal charge transport with both spatial inversion symmetry breaking and time reversal symmetry breaking<sup>8</sup>. In this case, the longitudinal resistance exhibits a unique directional response depending on the current and magnetic field directions. A phenomenological expression for this directional transport is expressed by generalizing Onsager's theorem as follows<sup>9,10</sup>

$$R(B, I) = R_0(1 + \beta B^2 + \gamma BI) \quad (1)$$

where  $R_0$ ,  $\beta$ ,  $\gamma$ ,  $I$  and  $B$  represent the resistance at zero magnetic field, the coefficient of the normal magnetoresistance (MR), the nonreciprocal transport coefficient, electric current and the external in-plane magnetic field perpendicular to  $I$ , respectively. Experimentally, nonreciprocal charge transport has been demonstrated in a variety of low-symmetry systems, including topological insulators/semimetals<sup>11-14</sup>, polar semiconductors<sup>15,16</sup>, semiconductor heterostructures<sup>17</sup>, superconducting systems<sup>18-21</sup> and correlated oxide heterostructures<sup>22-24</sup>. Achieving a high magnitude of this directional charge transport is of vital importance towards next-generation two-terminal rectification and spin-orbitronic devices<sup>20,25</sup>. To date, considerable efforts have been devoted to achieving the larger  $\gamma$  value via gate bias<sup>17,22</sup> and ionic-liquid gating<sup>26</sup>. However, these electric field-effect gating means remain highly limited to manipulate the Rashba spin-orbit coupling (SOC) strength and the Fermi level due to the relatively weak carrier tunability<sup>22</sup>, thus seriously restricting the  $\gamma$  enhancement.

Optical control is a paramount tool to explore emergent quantum phenomena in quantum materials<sup>27</sup>. In addition to ultrafast laser pulses, conventional light source has

also been proved to be a powerful tool to manipulate quantum phases, such as light-induced superconductivity in an organic Mott insulator<sup>28</sup>, light-induced insulator-metal transition in an ultrathin SrRuO<sub>3- $\delta$</sub> <sup>29</sup>, and optical modulation of Rashba SOC in two-dimensional electron gases (2DEGs) at SrTiO<sub>3</sub>-based interfaces<sup>30</sup>. It is highly desirable to unveil the sophisticated interplay between light and nonreciprocal transport. In this regard, however, light-induced nonreciprocal transport in quantum materials has remained largely unexplored yet.

As a *5d* transition-metal oxide, KTaO<sub>3</sub> (KTO)-based interfaces hosting 2DEGs have aroused considerable interest owing to fascinating physical properties, such as 2D anisotropic superconductivity<sup>31-34</sup>, tunable strong Rashba SOC<sup>35-39</sup>, and robust spin polarization<sup>40</sup>. Especially, the superconductivity at KTO-based interfaces is strongly dependent on the crystalline orientation of KTO with the highest superconducting transition temperature ( $T_c$ ) of 2.2 K at (111)-oriented surface<sup>31</sup>, very different from SrTiO<sub>3</sub>-based counterparts, indicating the underlying rich physics in KTO. Furthermore, the interfacial superconductivity can be further manipulated by the electric field with/without ionic-liquid gating, unveiling the electron-doped surface<sup>41</sup>. Specifically, KTO-based 2DEGs are also very sensitive to the conventional light source<sup>35,42,43</sup>, providing an ideal platform to explore the complicated interplay between photoelectrons and heavy *5d* electrons, thus readily tuning the Rashba SOC strength in a broader range under light illumination. However, the nonreciprocal charge transport via optical modulation in the KTO-based 2DEGs still remains elusive.

In this article, we demonstrate a light-induced giant enhancement of nonreciprocal transport at superconducting and epitaxial CaZrO<sub>3</sub>/KTO (111) (CZO/KTO) heterostructures grown by pulsed laser deposition (PLD). The magnitude of the nonreciprocal coefficient ( $\gamma$ ) undergoes a huge enhancement of 1000 times to  $10^5$  A<sup>-1</sup>T<sup>-1</sup> when illuminated at 330 nm. The Rashba SOC strength also experiences a remarkable increase, which is accompanied by the prominent photocarriers excited from the valence band of KTO. Combining first-principles calculations and data fitting, the giant

$\gamma$  enhancement is attributed to the larger Rashba coefficient and the longer carrier relaxation time under ultraviolet light illumination. Our work not only demonstrates the interplay between light and nonreciprocal transport, but also provides great potential for the realization of emergent two-terminal rectification devices and spin-orbitronic devices.

## Results

### Formation of high-quality 2DEGs at the CZO/KTO heterointerfaces

The CZO/KTO heterostructured films are prepared by depositing CZO films on (111)-oriented KTO single-crystal substrates by the PLD (see Methods for details). Figure 1a schematically shows the typical perovskite crystal structure for CZO/KTO heterostructures. The lattice parameter of CZO is very close to that of KTO with a lattice mismatch of only  $\sim 0.6\%$ . This is beneficial to a layer-by-layer epitaxial growth of the CZO/KTO perovskite heterostructures. Such a perfect epitaxy is indicated from the coincident diffraction peak of CZO from x-ray diffraction (XRD) (Supplementary Fig. 1a). The microstructure of the heterointerface is further examined by high-resolution scanning transmission electron microscopy (STEM) in a high angle annular dark field (HAADF) mode. From the STEM-HAADF image (Fig. 1b), it can be seen that the homogeneous and crystalline phase of CZO thin film is perfectly grown on the KTO (111) substrate. The enlarged atomic configuration overlapping on the STEM image is shown in Supplementary Fig. 1b. The corresponding energy dispersive x-ray spectroscopy (EDX) elemental mapping (Fig. 1c) indicates the clear and smooth interface between the KTO substrate and the CZO film without elemental interdiffusion. Note that the noticeable Ca element in the KTO substrate and K element in the CZO film (Fig. 1c) are actually an artifact due to the very close energy edges of Ca and K from EDX (Supplementary Fig. 2).

The transport properties are measured with a Hall-bar configuration (upper inset of Fig. 1d). The detailed fabrication process of the Hall-bar device is presented in

Supplementary Fig. 3. We observe a typically metallic behavior in the whole temperature range (Fig. 1d), indicating the formation of 2DEGs at their heterointerface. This is ascribed to the formation of oxygen vacancies at the surface of KTO<sup>44</sup>. The homogeneous conducting channel is evidenced by the arbitrarily selected multi-electrode measurements (Supplementary Fig. 4a). The anisotropic MR further reveals its 2D conducting characteristic with the thickness of around 4.35 nm (Supplementary Fig. 4b). Remarkably, the sheet resistance ( $R_s$ ) undergoes a rapid transition to a zero-resistance state when the temperature further decreases (see the lower inset of Fig. 1d), indicating the occurrence of superconductivity at the interface. The  $T_C$  is determined to be 0.43 K, which is defined by the temperature corresponding to 50% of the resistance according to the previous work<sup>31,32,44</sup>. Its  $T_C$  is much lower than those of non-epitaxial KTO-based heterointerfaces<sup>31,32</sup>, but comparable to that of epitaxial LaVO<sub>3</sub>/KTO (111) system ( $\sim 0.5$  K)<sup>45</sup>. Figure 1e depicts the field-dependent MR ( $\text{MR} = \frac{R(B) - R_0}{R_0} \times 100\%$ ) and Hall resistance ( $R_{xy}$ ) at 5 K. The MR rapidly decreases to a minimum, forming a cusp shape at the low field and manifesting a notable characteristic of weak antilocalization (WAL). The emergence of the WAL effect implies the non-negligible contribution of the Rashba SOC<sup>37,46</sup>. Besides, the linear behavior of  $R_{xy}$  with a negative slope indicates that the charge carriers are electrons and only one type of carriers dominates the transport. The temperature-dependent carrier density ( $n_s$ ) and the Hall mobility ( $\mu$ ) extracted from the Hall curves are shown in Fig. 1f. The  $n_s$  is  $4.6 \times 10^{13}$  cm<sup>-2</sup> at 300 K and decreases to a constant value of  $\sim 3.8 \times 10^{13}$  cm<sup>-2</sup> at low temperatures. This is recognized as a carrier freezing-out effect due to the in-gap states generated by oxygen vacancies<sup>30,47,48</sup>. Meanwhile, the carrier mobility decreases from 140 cm<sup>2</sup> V<sup>-1</sup> s<sup>-1</sup> at 2 K to 14 cm<sup>2</sup> V<sup>-1</sup> s<sup>-1</sup> at 250 K due to the lattice vibration, consistent with the previous report on the EuO/KTO (110) heterointerfaces<sup>49</sup>.

### **Giant enhancement of nonreciprocal transport under ultraviolet irradiation**

In order to have a comprehensive understanding of the photoresponse of the CZO/KTO

heterointerface, we initially illuminate the sample with the conventional light source at wavelengths ( $\lambda$ ) of 300-700 nm at 5 K. The Hall-bar device is totally covered by the light, as schematically illustrated in Fig. 2a. Prior to systematic light-controllable experiments, the light-induced and large-current-induced heating effects are both ruled out, and amorphous-LaMnO<sub>3</sub> (a-LMO)/KTO interface maintains insulating during the light illumination (Supplementary Fig. 5), ensuring the intrinsic nature of 2DEGs during light-irradiation transport measurements. The resistance at 5 K firstly decreases by  $\sim 7\%$  upon 700-nm illumination, and then shows no significant change in the wavelength range of 700 to 450 nm due to the low photon energy (Fig. 2b), which largely determines the average location ( $\sim 2.3$  eV) of the existing in-gap state (Fig. 2c). Furthermore, a notable reduction of  $R_s$  is observed upon the exerted photon energy between 2.82 and 3.45 eV (i.e.,  $360 \text{ nm} \leq \lambda \leq 440 \text{ nm}$ ), which largely determines the average location ( $\sim 3.1$  eV) of the other in-gap state (Fig. 2c). The electrons residing in these two in-gap states generated from oxygen vacancies can be both excited to the conduction band minimum (CBM), thus increasing the conductivity<sup>50,51</sup>. Particularly, as the wavelength continues to reduce,  $R_s$  undergoes a sharp decrease and reaches a minimum at 330 nm (Fig. 2b). This photon energy of  $\sim 3.76$  eV is just slightly greater than the KTO's bandgap energy ( $\sim 3.6$  eV), thus capable of pumping abundant electrons from the valence band maximum (VBM) to the CBM. The final increase in  $R_s$  upon 300-nm illumination is noteworthy. In this case, the electrons in the VBM are excited to the higher subbands in the conduction band due to the larger photon energy ( $\sim 4.14$  eV). These photocarriers lead to increased interactions between electrons and the lattice (phonons), which results in a longer time for the electrons to return to a lower energy state. During this enhanced relaxation process, more photogenerated electrons would experience a notable competition between the weak localization and WAL upon the 300-nm excitation (see the next section) in addition to the likely recombination of photogenerated electrons and holes, thus resulting in a decrease in the total carrier density responsible for conductivity and ultimately an increase in  $R_s$ .

Since the CZO/KTO shows the distinct photoresponse at different wavelengths, we select light with specific wavelengths to control the nonreciprocal transport. The measurements are carried out with an exerted small direct current ( $I = \pm 40 \mu\text{A}$ ) at 5 K with simultaneously applying an in-plane magnetic field normal to the current direction. The current-direction-dependent in-plane MR under illumination is displayed in Fig. 2d. The heterostructure shows a relatively weak nonreciprocal response at  $\lambda \geq 500 \text{ nm}$  and in the dark, implying an indistinctive excitation at long wavelengths. This is coincident with the case revealed by the  $\lambda$ -dependent  $R_s$  measurements (Fig. 2b). With the decreasing  $\lambda$ , a distinct noncoincidence of MR emerges. Remarkably, when illuminated at 330 nm, a significant misalignment of MR is clearly seen upon reversing the current direction, showing a giant enhancement of nonreciprocal transport. We plot the ratio of the resistance change ( $\Delta R/R_0$ ) as a function of the magnetic field in between  $+I_x$  and  $-I_x$  (Fig. 2e), where the  $\Delta R$  represents the difference in resistance upon opposite directions of the currents and  $R_0$  represents the longitudinal resistance at zero field. Compared to the dark case, an amplified signal of unidirectional resistance with the magnitude of around 4% is observed owing to the notable gating effect at 330 nm. Besides, the  $\Delta R/R_0$  exhibits a linear dependence on the magnetic field as well as the applied current (Supplementary Fig. 6) near the origin, which is known as bilinear magnetoresistance (BMR). The BMR is fitted well with the above-mentioned phenomenological expression (equation 1) and has been widely discovered in other noncentrosymmetric systems<sup>23,24</sup>. Meantime, the  $\Delta R/R_0$  undergoes a gradual saturation with increasing field, which is likely attributed to the complex effect of the large Zeeman energy exerting on the band structures<sup>52,53</sup>. Moreover, the nonreciprocal transport gradually weakens with increasing temperature and vanishes at around 40 K, which is attributed to the disruption of spin-momentum locking by quantum fluctuations (Supplementary Fig. 7). In addition, we also perform the second harmonic measurements to further confirm the light-induced giant enhancement of nonreciprocal transport at KTO (111)-based interfaces (Supplementary Fig. 8).



The nonreciprocal coefficient  $\gamma = \Delta R/(2BIR_0)$  is derived from the phenomenological equation (1), which is used as the main figure of merit to quantify the nonreciprocal transport. Since  $\Delta R/R_0$  exhibits an excellent linear dependence in  $\pm 0.7$  T range, we apply this field range to attain  $\gamma$ . Its evolution with light wavelength is plotted in Fig. 2f. In the dark, the  $\gamma$  is estimated to be  $\sim 10^2 \text{ A}^{-1}\text{T}^{-1}$ , which is comparable to that in  $\text{LaAlO}_3/\text{SrTiO}_3$  heterostructures<sup>22</sup> and much larger than those observed in other asymmetric systems, such as  $\text{BiTeBr}$ <sup>26</sup>,  $\alpha\text{-GeTe}$ <sup>15</sup> and  $\text{Bi}_2\text{Se}_3$ <sup>54</sup>. Very strikingly, the  $\gamma$  increases rapidly to  $\sim 10^5 \text{ A}^{-1}\text{T}^{-1}$  under 330-nm irradiation, almost three orders of magnitude larger than that in the dark. This giant  $\gamma$  value in 2DEGs is notably comparable to those in complex topological insulator nanowires<sup>53</sup> and noncentrosymmetric superconductors<sup>55</sup>, further establishing the giant tunability of optical control in our nonreciprocal transport. To highlight the giant enhancement of nonreciprocal transport by light control, we summarize the nonreciprocal transport coefficient modulated by various methods, such as electric-field control and ionic-liquid gating in Fig. 2g. It is seen that our light-control method clearly distinguishes itself from this benchmark chart in terms of both the giant  $\gamma$  and the extraordinary tunability.

### **Light-induced enhancement of Rashba SOC strength and photocarrier excitation**

Why does light have such a superior manipulation capacity of nonreciprocal transport? To further reveal the underlying physical picture, we carried out MR and Hall-effect measurements by applying an out-of-plane magnetic field with the identical wavelengths. As shown in Fig. 3a, MR and  $R_{xy}$  maintain constant at  $\lambda = 700, 600,$  and  $500$  nm as compared to the dark condition, consistent with the above results of  $\lambda$ -dependent  $R_s$  and nonreciprocal transport (Fig. 2b,d). Under 400-nm illumination, MR shows a modest increase and the Hall effect experiences a linear to nonlinear transition due to the excitation of electrons from in-gap states. Remarkably, a much stronger WAL effect emerges at 330 nm, implying a giant Rashba SOC strength. Besides, Hall curve

becomes apparently nonlinear. Two distinct slopes can be traced at low and high magnetic fields, respectively, which is a featured behavior of Hall effect contributed by two types of carriers<sup>56</sup>. It is noteworthy that the WAL effect and nonlinear Hall characteristic are simultaneously suppressed when the wavelength decreases to 300 nm, and the competition between the weak localization and WAL becomes notable, which is due to the same physical mechanism as the  $R_s$  increase (Fig. 2b). We do not observe any hysteresis in the MR and Hall curves under 330-nm irradiation (Supplementary Fig. 9), indicating that light irradiation cannot induce any spin polarization in KTO-based 2DEGs. It is apparent that there is a close connection among the light-induced MR change, Hall effect and nonreciprocal transport.

To quantify the Rashba SOC tuned by different wavelengths, the WAL effect is analyzed by employing the modified Maekawa-Fukuyama (MF) theory<sup>57,58</sup>, which has been proved to be well applicable in 2DEGs at oxide heterointerfaces<sup>59</sup>. We present the magnetoconductance  $\Delta\sigma(B) = \sigma(B) - \sigma(0)$  in the unit of the quantum conductance ( $G_Q = 2e^2/h$ ) under different wavelengths, where  $\sigma(0)$  is the magnetoconductance at zero field (Fig. 3b). The total magnetoconductance under the negligible Zeeman splitting can be written as<sup>57,58</sup>

$$\begin{aligned} \frac{\Delta\sigma(B)}{G_Q} = & -\frac{1}{2}\Psi\left(\frac{1}{2} + \frac{B_i}{B}\right) + \Psi\left(\frac{1}{2} + \frac{B_i+B_{so}}{B}\right) - \ln\left(\frac{B_i+B_{so}}{B}\right) \\ & + \frac{1}{2}\Psi\left(\frac{1}{2} + \frac{B_i+2B_{so}}{B}\right) - \frac{1}{2}\ln\left(\frac{B_i+2B_{so}}{B_i}\right) - \frac{AB^2}{1+CB^2} \end{aligned} \quad (2)$$

where  $\Psi(x)$  is the digamma function, and  $B_i$  and  $B_{so}$  are the inelastic scattering and the SOC effective fields, respectively. These two characteristic fields are introduced to characterize  $B$ -dependent quantum correction based on the inelastic scattering and SOC scattering processes. The last term is from the Kohler's rule, which describes the ordinary magnetoconductance with fitting parameters of  $A$  and  $C$ . The fitting  $B_{so,i}$  results are displayed in Fig. 3c. Obviously,  $B_{so}$  reaches a maximum of 14.7 T at 330 nm, suggesting a greatly enhanced Rashba SOC strength. Note that the  $\lambda$ -dependent  $B_{so}$  evolution is consistent with that of the  $\lambda$ -dependent  $R_s$  (Fig. 2b), indicating their inherent direct relation and the same physical mechanism. In contrast, the inelastic

scattering field ( $B_i$ ) displays a gradual increase with increasing wavelength and is much smaller than the SOC field when  $\lambda \leq 400$  nm (Fig. 3c), implying the predominant role of the WAL effect. Other deduced parameters (i.e., spin relaxation length, dephasing length, spin relaxation time, inelastic scattering time, Rashba coefficient and spin-splitting energy) are provided in Supplementary Fig. 10 to shed more light on the light-tunable Rashba SOC. When calculating the Rashba coefficient and spin-splitting energy, the effective mass  $m^*$  takes  $0.3m_0$  (where  $m_0$  is the free electron mass) according to the previous angle-resolved photoemission spectroscopy (ARPES) experimental result<sup>60</sup>. It should be noted that the Rashba coefficient ( $\alpha_R$ ) reaches the maximum value of  $0.26$  eV Å, largely comparable with that deduced from the ARPES experiment<sup>38</sup>. The largest spin-splitting energy ( $\Delta$ ) can also reach  $167.9$  meV, which is a typically high record among Rashba interfacial systems. Such a highly tunable capacity by light manifests the potential applications of KTO-based interfaces in the energy-efficient opto-spintronic devices.

Furthermore, the two-band model is performed to extract the carrier density and mobility from Hall measurements to figure out the electron excitation process<sup>30,35</sup>:

$$R_{xy}(B) = -\frac{1}{e} \frac{\left(\frac{n_1\mu_1^2}{1+\mu_1^2B^2} + \frac{n_2\mu_2^2}{1+\mu_2^2B^2}\right)B}{\left(\frac{n_1\mu_1}{1+\mu_1^2B^2} + \frac{n_2\mu_2}{1+\mu_2^2B^2}\right)^2 + \left(\frac{n_1\mu_1^2}{1+\mu_1^2B^2} + \frac{n_2\mu_2^2}{1+\mu_2^2B^2}\right)B^2} \quad (3)$$

with the constraint of

$$R_0 = \frac{1}{e(n_1\mu_1 + n_2\mu_2)} \quad (4)$$

where  $n_{1,2}$  denote the first- and second-type sheet carriers at the CZO/KTO interface, respectively,  $\mu_{1,2}$  are the corresponding Hall mobilities, and  $e$  is electron charge. The fitting curves are depicted in Supplementary Fig. 11 and the fitting parameters are presented in Fig. 3d,e. In the region of  $\lambda > 400$  nm, the intrinsic electrons ( $n_1$ ) dominate exclusively for the conductivity with a mobility of  $162$  cm<sup>2</sup>V<sup>-1</sup>s<sup>-1</sup>. Nevertheless, a second type of carriers begins to emerge when  $\lambda \leq 400$  nm. Remarkably, the carrier density ( $n_2$ ) and mobility ( $\mu_2$ ) of the second-type carriers both undergo a giant increase at  $330$  nm to  $0.3 \times 10^{13}$  cm<sup>-2</sup> and  $15400$  cm<sup>2</sup>V<sup>-1</sup>s<sup>-1</sup>, respectively, which stems from the

photoelectrons excited from the KTO's VBM under the significant light-excitation process (Fig. 2c). The Lifshitz transition is thus believed to occur at about 400-nm irradiation (Fig. 3d,e). It is noted that the carrier density of  $n_1$  undergoes an unexpected increase to  $1.6 \times 10^{14} \text{ cm}^{-2}$  at 330 nm, which is very different from the previous observation on the optical gating of oxide 2DEGs where the intrinsic carrier  $n_1$  keeps almost constant under illumination<sup>35</sup>. This phenomenon is attributed to the fact that the photocarriers tend to fill the Ta- $t_{2g}$  CBM where the intrinsic carrier occupies, thus increasing  $n_1$  remarkably (Supplementary Fig. 12). The sudden decrease in carrier density ( $n_{1,2}$ ) and mobility ( $\mu_2$ ) with 300-nm excitation is also ascribed to the notable competition between the weak localization and WAL as well as the likely recombination of photogenerated electrons and holes, in good agreement with the  $R_s$  increase (Fig. 2b). This gives us a comprehensive and in-depth understanding of the complex interplay between light and electron excitation process at the CZO/KTO heterointerfaces, which helps to figure out the origin behind the giant  $\gamma$  enhancement.

### Theoretical analyses

In order to disclose the nature of such a giant enhancement of nonreciprocal transport, we perform the density functional theoretical (DFT) calculations on 2DEGs occurring at the surface of KTO (111) (see Methods for details). The prominent Rashba spin splitting is observed near  $\Gamma$  point in the calculated electronic band structure (Fig. 4a). Note that there is no significant difference among calculated electronic band structures of KTO under different Hubbard  $U$  values (3-5 eV), suggesting that light only impacts on the location of  $E_F$  (Supplementary Fig. 13), thereby influencing the Rashba SOC strength as well as the nonreciprocal transport. Representative Fermi surfaces with  $E_F = 0.03$  and 0.25 eV are displayed in Fig. 4b,c, which are marked with the dashed black and red lines (Fig. 4a), respectively. These two Fermi surfaces denote the dark and 330-nm illumination conditions, respectively. In the dark condition, the electronic band filling is low ( $E_F = 0.03$  eV). Thus, a Fermi contour is obtained where the Rashba spin-

splitting energy ( $\Delta$ ) is relatively small with  $\Delta = 35$  meV (Fig. 4b). Upon illumination with 330-nm light, the significant photoexcitation process brings about a sharp increase in band filling ( $E_F = 0.25$  eV). In this regard, the Fermi level crosses the bottom of the upper subband, and a complicated pattern of Fermi contour is obtained with the larger  $\Delta$  ( $\Delta_1 = 310.9$  meV for Band 1,2 and  $\Delta_2 = 125.9$  meV for Band 3,4) (Fig. 4c). As depicted in Fig. 4d, the calculated average  $\bar{\alpha}_R$  exhibits a strong dependence on the  $E_F$  for Band 1,2. When subjected to illumination at 330 nm, abundant photocarriers start to fill the additional Ta- $t_{2g}$  conduction band (Supplementary Fig. 12). Thus, the  $\bar{\alpha}_R$  contributed by all the bands increases nearly one order of magnitude as compared to that in the dark (Fig. 4d), which should contribute to the larger  $\gamma$  in view of the criterion of  $\gamma \propto \alpha_R \tau^2 / E_F^{23}$ . Here, the nonreciprocal transport coefficient  $\gamma$  is derived from the underlying physical picture of the nonreciprocal transport<sup>23</sup> rather than the direct phenomenological equation (1)<sup>9,10</sup>.

Furthermore, the second type of photocarriers has the remarkably high mobility (Fig. 3e), which is mainly excited to Band 3,4 of the Ta 5d  $t_{2g}$  orbitals ( $d_{xy}$ ,  $d_{xz}$  and  $d_{yz}$ ) that are highly degenerate. Its high mobility leads to the longer relaxation time  $\tau$ , which also contributes to the giant  $\gamma$  enhancement. Given that the magnitude of  $\tau$  is not apt to be estimated from mobility with two types of carriers, we adopt the quadratic magnetoresistance (QMR) to fit it (Fig. 4e). The QMR is defined as  $[\text{MR}(B, +I_x) + \text{MR}(B, -I_x)]/2$ , and it is fitted by the following expression<sup>23</sup>:

$$\text{QMR} = \frac{3}{4} \left( \frac{g\mu_B}{\hbar} \right)^2 \tau^2 B^2 \quad (5)$$

where  $\frac{3}{4} \left( \frac{g\mu_B}{\hbar} \right)^2 \tau^2$  is defined as  $A_{\text{QMR}}$ ,  $g$  is the  $g$ -factor,  $\mu_B$  is the Bohr magneton, and  $\hbar$  is the reduced Plank constant. Since the  $A_{\text{QMR}}$  is independent on  $\alpha_R$  and  $E_F$ , the  $\tau$  can be deduced from  $A_{\text{QMR}}$ . It is seen that the  $\tau$  at 330 nm increases ten times than that in the dark (Fig. 4f). Consequently, it is a synergistic effect resulting from both the light-induced increased Rashba SOC strength and the prolonged relaxation time that eventually boosts the substantial enhancement of nonreciprocal charge transport at KTO (111)-based interfaces.

## Discussion

In summary, we have achieved a giant enhancement of nonreciprocal charge transport via optical gating at the Rashba heterointerfaces of CZO/KTO. The conventional light source with a specific wavelength of 330 nm pumps abundant electrons from the valence band of KTO to the Ta- $t_{2g}$  conduction band, thus bringing about the stronger Rashba SOC strength as well as additional high-mobility photocarriers. Thanks to the above remarkable photodoping effect, the nonreciprocal transport coefficient  $\gamma$  experiences three orders of magnitude increase up to  $\sim 10^5$  A<sup>-1</sup>T<sup>-1</sup>, which is well confirmed by DFT theoretical calculations. Our work not only provides an alternative approach to control the nonreciprocal transport by the external light stimulus in various Rashba systems, but also overcomes the bottleneck of previous methods to facilitate the potential applications in opto-rectification devices and spin-orbitronic devices.

## Methods

### Film fabrication

The films were fabricated on  $5 \times 5$  mm<sup>2</sup> (111) KTO single-crystal substrates by the PLD technique using 248-nm KrF laser with a fluence of 2 J cm<sup>-2</sup> and the repetition rate of 1 Hz. Before film growth, the substrates were cleaned with acetone, alcohol and deionized water successively. The Hall-bar device was fabricated by optical lithography using a hard mask made from a-LMO with width of 50  $\mu$ m and length of 500  $\mu$ m. The 50-nm-thick CZO films were epitaxially deposited at 750 °C with the oxygen pressure of 10<sup>-5</sup> mbar. After deposition, the films were cooled down to room temperature at 5 °C per minute under the same oxygen pressure.

### Structural characterization

The crystal structure of the films was measured by  $\theta$ -2 $\theta$  XRD in a high-resolution mode using Cu- $K_\alpha$  emission (1.5418 Å, Bruker D8 Discover). The cross-sectional specimen

for STEM-HAADF was prepared on a ZEISS Crossbeam 550L electron beam/focused ion beam electron microscopy at 1-30 kV. The high-resolution STEM images were collected by the aberration-corrected microscope operated at 200 kV (JEOL ARM 200F). For STEM-HAADF imaging, the semi-convergent angle of the probe forming lens was set to 25 mrad. The EDX mapping was acquired from 2 silicon drift detector system.

### **Light-irradiation transport measurements**

Prior to the light-irradiation transport measurements, electrodes were bonded with aluminum wires using an ultrasonic wire bonder. The standard eight-probe configuration (Fig. 2a) was used for the transport characterization through a 12 T Cryogenic cryogen-free measurement system (CFMS-12). Keithley 6221 and 2182 nanovoltmeters were employed for current source and voltage source detection, respectively. To study the effect of light control during the transport measurements, we used a tunable conventional xenon light source with the wavelength ranging from 300 to 700 nm. The light beam was guided into the CFMS transport system through the sample holder rod attached with a quartz optical fiber. When the heterostructure was exposed to the light, the light absorption in the upper CZO layer was negligible due to its wide-bandgap property and transparent nature. The light power density was maintained a constant value of  $\sim 0.3 \text{ mW cm}^{-2}$  for all the wavelengths to avoid any light-induced heating effect. Notably, after each circle of the light irradiation with a certain wavelength, CZO/KTO heterostructures were warmed up to the room temperature to restore the initial state. Thus, the persistent photoconductivity could be ruled out. In addition, we performed the light-controlled experiments after waiting for enough time to stabilize the resistance every time. As the nonreciprocal transport is more pronounced at low temperatures the temperature for the transport measurements was mainly set at 5 K.

## First-principles calculations

We performed the DFT first-principles calculations upon electronic properties of KTO of slab models by employing the Vienna ab initio simulation package (VASP)<sup>61,62</sup>. A slab model of 12 Ta-layers on the (111) surface was considered. We adopted the generalized gradient approximation (GGA) with the Perdew-Burke-Ernzerhof<sup>63,64</sup> type exchange-correlation potential with the energy cutoff fixed to 450 eV. By considering the transition metal Ta, GGA plus Hubbard  $U$  functions with  $U = 3, 4$  and  $5$  eV were applied for Ta- $d$  orbitals for all the results. Total Hellmann-Feynman forces were taken to  $10^{-2}$  eV  $\text{\AA}^{-1}$  for the structural optimization.  $6 \times 6 \times 1$   $\Gamma$ -centered  $k$ -points sampling was used in the primitive unit cells. A total energy tolerance  $10^{-7}$  eV was adopted for self-consistent convergence. The SOC was included in self-consistent calculations and energy band calculations. In order to obtain the Fermi surface, we used the maximally localized Wannier functions (MLWF) from the first-principles calculations<sup>65,66</sup> to set up MLWF-based tight-binding Hamiltonians. The Ta- $d$ , O- $p$  orbitals were initialized for MLWFs by Wannier90<sup>67</sup>. We calculated the average Rashba coefficients from the energy spectrum

$$\bar{\alpha}_R = \frac{\hbar^2 \Delta \bar{k}}{2m^*} \quad (6)$$

where  $\Delta \bar{k} = \bar{k}_{\text{in}} - \bar{k}_{\text{out}}$  is the difference of two neighboring subbands, and  $m^*$  is the electron effective mass.

## Acknowledgements

This work was supported by the National Key Research and Development Program of China (grant no. 2022YFA1402404 to X.W.) and the National Natural Science Foundation of China (grant nos. T2394473, T2394470, 62274085, 11874203 and 61822403 to X.W. and grant nos. 92161201 and 12025404 to F.S.).



### **Author contributions**

X.W. conceived the study and proposed the strategy. X.W. and R.Z. supervised the project. X.Z. and Z.C. grew the samples and performed XRD measurements. T.Z. and H.Z. conducted theoretical calculations. Y.T. and B.G. carried out the microscopic characterization. X.Z., A.S., C.Z. and R.G. fabricated the devices and performed transport measurements. G.L. and J.S. performed superconductivity measurements. S.Z., W.N., Y.C., F.F., W.L., K.C., F.S. and R.Z. contributed to the data analysis and discussion. X.W. and X.Z. wrote the manuscript with input from all the authors. All authors contributed to manuscript revisions.

### **Competing interests**

The authors declare no competing interests.

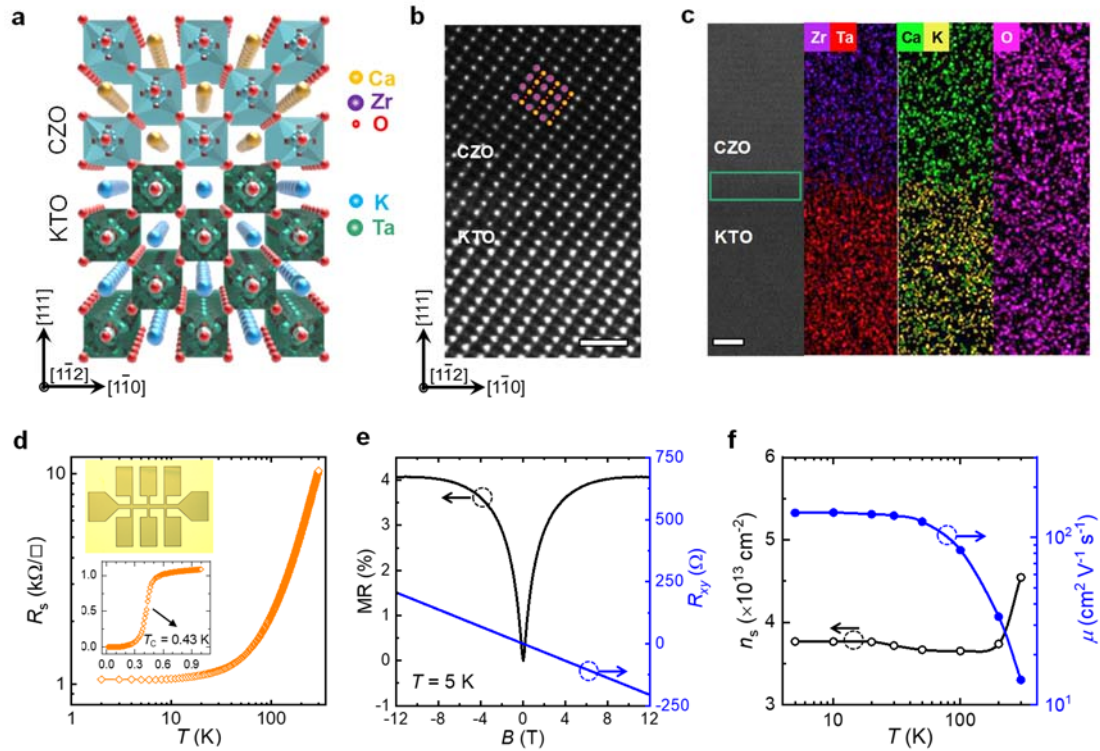


**Fig. 1 | Basic structural and transport properties.** **a** Schematic illustration of the crystal structure for the perovskite heterostructures of CZO/KTO. **b** STEM-HAADF image of CZO/KTO, overlapped with the atomic configuration. The scale bar is 1 nm. **c** STEM image and the corresponding EDX elemental mapping at the interface. The green box indicates the area where 2DEGs are located at the interface. The scale bar is 5 nm. **d** Temperature-dependent sheet resistance ( $R_s$ ) of the CZO/KTO heterostructure. The upper inset shows the optical image of the Hall-bar device. The lower inset indicates the superconductivity observed at cryogenic temperature. **e** MR and Hall resistance ( $R_{xy}$ ) with respect to the applied out-of-plane magnetic field at 5 K. **f** Temperature-dependent carrier density ( $n_s$ ) and mobility ( $\mu$ ) of the device without illumination.

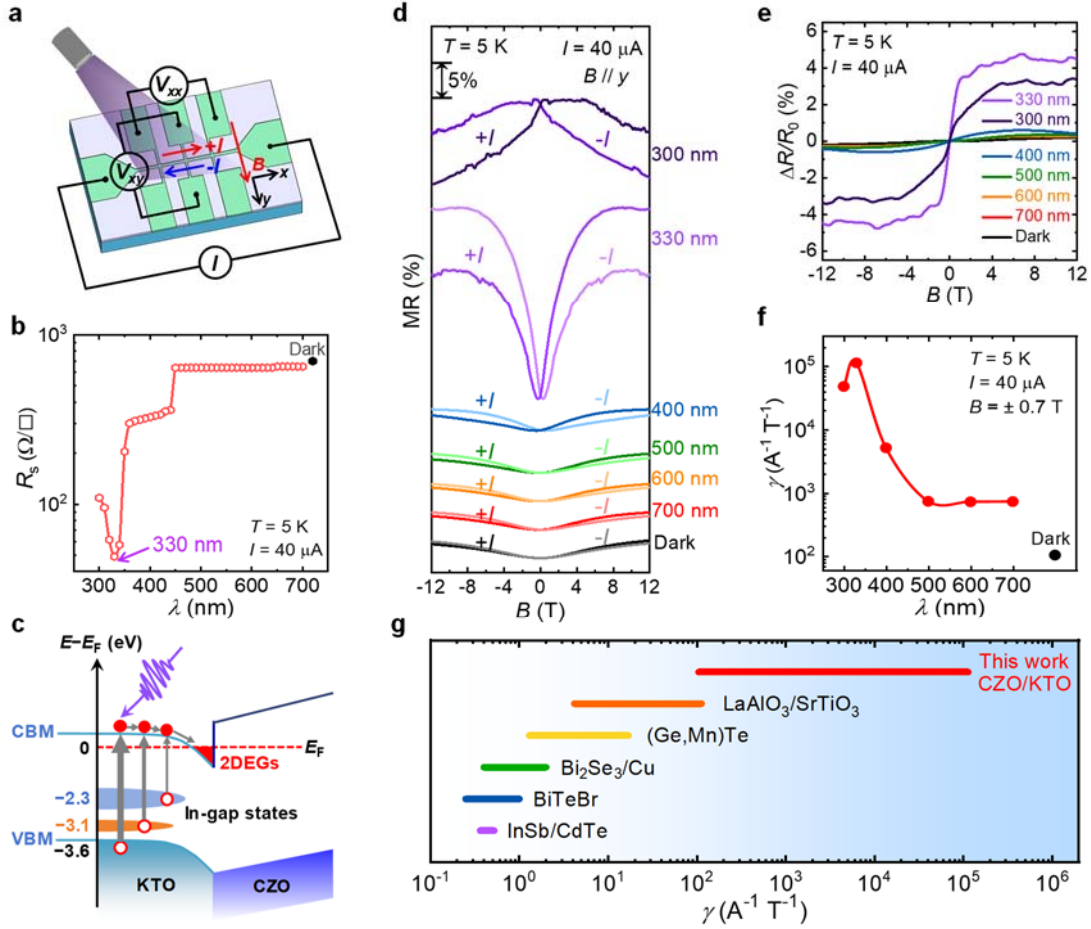


**Fig. 2 | Light-induced giant enhancement of nonreciprocal transport.** **a** Schematic measurement configuration diagram of the optical modulation for the Hall-bar device of 2DEGs at the CZO/KTO heterointerface. Note that the in-plane magnetic field is perpendicular to the current direction. **b** Photoinduced change of the resistance of 2DEGs as a function of the incident light wavelength at 5 K, showing that the irradiation at 330 nm with the energy ( $\sim 3.76$  eV) slightly exceeding the optical bandgap of KTO leads to the largest photoconductance. **c** Schematic band structure diagram of the light-gating mechanism at the CZO/KTO interface. The thicker grey arrows denote the more photoexcited electrons. **d** In-plane MR curves at various wavelengths. The measurements are performed for both  $I = \pm 40$   $\mu$ A at 5 K. The MR curves are shifted vertically for clarity. **e** The ratio of the resistance change ( $\Delta R/R_0$  extracted from **d**) as a function of magnetic field at various wavelengths. **f** Wavelength-dependent nonreciprocal transport coefficient extracted from **e**. The fitting range of the magnetic field is set to be  $\pm 0.7$  T. The corresponding curves and parameters of the dark condition are also included in **b, d-f** for comparison. **g** The summarized graph for  $\gamma$  of various material systems, such as InSb/CdTe<sup>17</sup>, BiTeBr<sup>26</sup>, Bi<sub>2</sub>Se<sub>3</sub>/Cu<sup>54</sup>, (Ge,Mn)Te<sup>16</sup> and LaAlO<sub>3</sub>/SrTiO<sub>3</sub><sup>22</sup>, that utilize various methods for the nonreciprocal transport modulation.

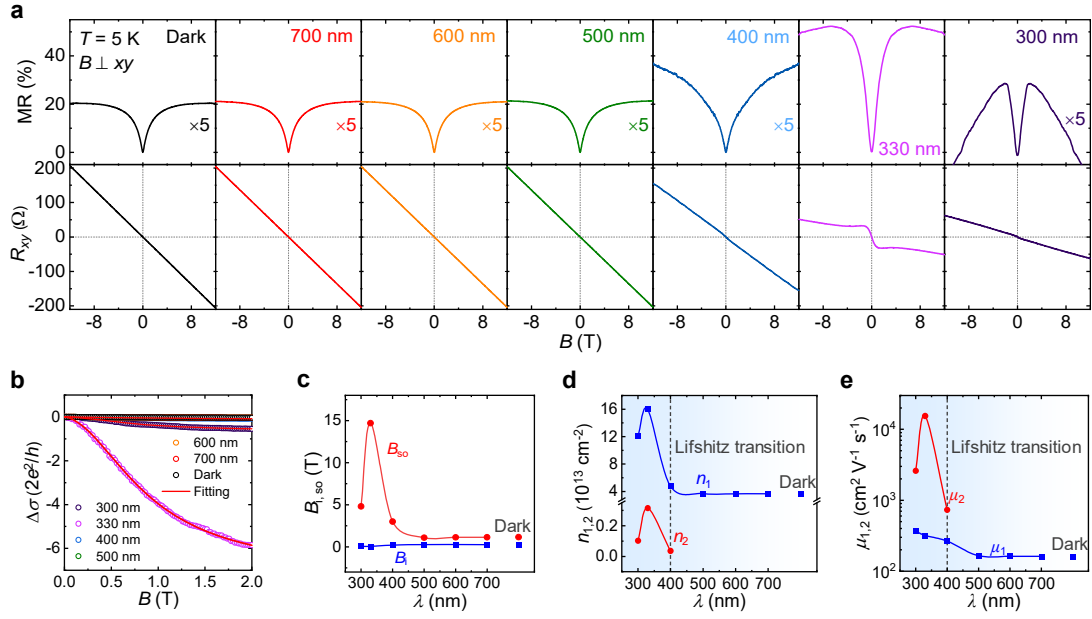


**Fig. 3 | Optical gating of the CZO/KTO heterointerface.** **a** The MR and Hall curves in the dark and under illumination with various wavelengths under the applied out-of-plane magnetic field at 5 K. **b** The magnetoconductance curves in the dark and at different wavelengths. The solid red curves are the best fits to the MF model. **c** The Rashba SOC effective field ( $B_{so}$ ) and inelastic scattering field ( $B_i$ ) extracted from **b** as a function of wavelength. **d,e** The derived carrier density ( $n_{1,2}$ ) and mobility ( $\mu_{1,2}$ ) from the Hall effect as a function of wavelength according to the two-band model. The dashed lines indicate the Lifshitz transition point. The corresponding parameters of the dark condition are also included in **c-e**.

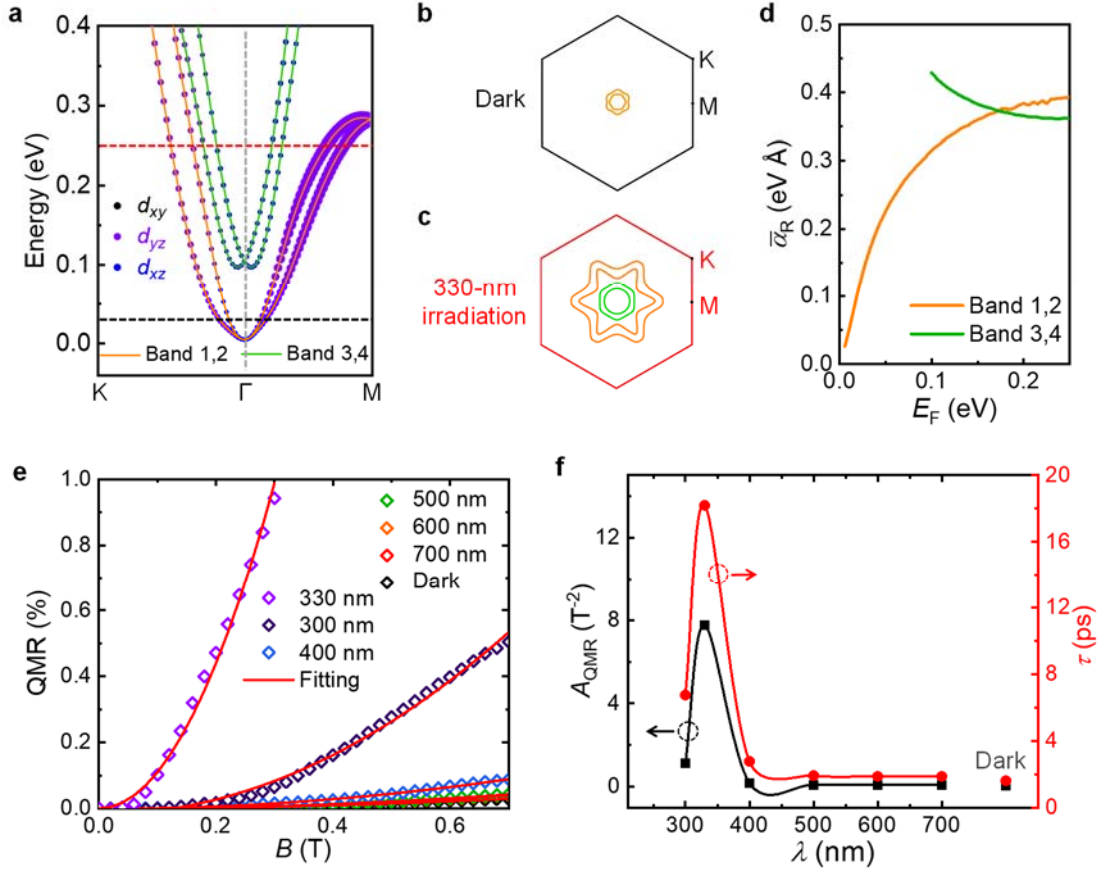


**Fig. 4 | Theoretical analyses for the light-induced enhancement of nonreciprocal transport.** **a** The calculated electronic band structure (Band 1-4, orange and green lines) and the weight of  $d_{xy}$ ,  $d_{yz}$  and  $d_{xz}$  (black, purple and blue circles) orbitals of 12-Ta layers of KTO (111) surface from first-principles calculations with Hubbard  $U = 4$  eV. The weight of the orbitals is expressed by the size of the corresponding circles. **b,c** The calculated Fermi surfaces at  $E_F = 0.03$  (in the dark) and  $0.25$  eV (with the 330-nm irradiation), which are indicated by the dashed black and red lines in **a**, respectively. **d** The average Rashba coefficient ( $\bar{\alpha}_R$ ) versus the  $E_F$  for bottom Band 1,2 (orange line) and top Band 3,4 (green line). **e** The QMR as a function of the in-plane magnetic field at various wavelengths and in the dark. The solid red curves are the best fits according to equation (5). **f**  $A_{\text{QMR}}$  and the relaxation time ( $\tau$ ) deduced from **e** as a function of wavelength. The corresponding parameters of the dark condition are also shown.

## References

1. Ideue, T. & Iwasa, Y. Symmetry breaking and nonlinear electric transport in van der Waals nanostructures. *Annu. Rev. Condens. Matter Phys.* **12**, 201-223 (2021).
2. Sodemann, I. & Fu, L. Quantum nonlinear Hall effect induced by Berry curvature dipole in time-reversal invariant materials. *Phys. Rev. Lett.* **115**, 216806 (2015).
3. Gao, A. Y. et al. Quantum metric nonlinear Hall effect in a topological antiferromagnetic heterostructure. *Science* **381**, 181-186 (2023).
4. Wang, N. Z. et al. Quantum-metric-induced nonlinear transport in a topological antiferromagnet. *Nature* **621**, 487-492 (2023).
5. Bhatnagar, A., Chaudhuri, A. R., Kim, Y. H., Hesse, D. & Alexe, M. Role of domain walls in the abnormal photovoltaic effect in BiFeO<sub>3</sub>. *Nat. Commun.* **4**, 2835 (2013).
6. Ganichev, S. D. et al. Conversion of spin into directed electric current in quantum wells. *Phys. Rev. Lett.* **86**, 4358-4361 (2001).
7. Chen, Z. et al. Defect-induced helicity-dependent terahertz emission in Dirac semimetal PtTe<sub>2</sub> thin films. Preprint at <https://arxiv.org/abs/2310.09989> (2023).
8. Tokura, Y. & Nagaosa, N. Nonreciprocal responses from non-centrosymmetric quantum materials. *Nat. Commun.* **9**, 3740 (2018).
9. Ideue, T. et al. Bulk rectification effect in a polar semiconductor. *Nat. Phys.* **13**, 578-583 (2017).
10. Rikken, G., Fölling, J. & Wyder, P. Electrical magnetochiral anisotropy. *Phys. Rev. Lett.* **87**, 236602 (2001).
11. He, P. et al. Bilinear magnetoelectric resistance as a probe of three-dimensional spin texture in topological surface states. *Nat. Phys.* **14**, 495-499 (2018).
12. Yokouchi, T., Ikeda, Y., Morimoto, T. & Shiomi, Y. Giant magnetochiral anisotropy in Weyl semimetal WTe<sub>2</sub> induced by diverging Berry curvature. *Phys. Rev. Lett.* **130**, 136301 (2023).
13. Zhang, Z. W. et al. Controlled large non-reciprocal charge transport in an intrinsic magnetic topological insulator MnBi<sub>2</sub>Te<sub>4</sub>. *Nat. Commun.* **13**, 6191 (2022).
14. Li, C. et al. Observation of giant nonreciprocal charge transport from quantum Hall edge states of single surface in topological insulator. Preprint at <https://arxiv.org/abs/2307.08917> (2023).
15. Li, Y. et al. Nonreciprocal charge transport up to room temperature in bulk Rashba semiconductor  $\alpha$ -GeTe. *Nat. Commun.* **12**, 540 (2021).
16. Yoshimi, R. et al. Nonreciprocal electrical transport in the multiferroic semiconductor (Ge,Mn)Te. *Phys. Rev. B* **106**, 115202 (2022).
17. Li, L. et al. Room-temperature gate-tunable nonreciprocal charge transport in lattice-matched InSb/CdTe heterostructures. *Adv. Mater.* **35**, 2207322 (2023).

18. Wakatsuki, R. et al. Nonreciprocal charge transport in noncentrosymmetric superconductors. *Sci. Adv.* **3**, e1602390 (2017).
19. Hoshino, S., Wakatsuki, R., Hamamoto, K. & Nagaosa, N. Nonreciprocal charge transport in two-dimensional noncentrosymmetric superconductors. *Phys. Rev. B* **98**, 054510 (2018).
20. Zhang, E. Z. et al. Nonreciprocal superconducting NbSe<sub>2</sub> antenna. *Nat. Commun.* **11**, 5634 (2020).
21. Masuko, M. et al. Nonreciprocal charge transport in topological superconductor candidate Bi<sub>2</sub>Te<sub>3</sub>/PdTe<sub>2</sub> heterostructure. *npj Quantum Mater.* **7**, 104 (2022).
22. Choe, D. et al. Gate-tunable giant nonreciprocal charge transport in noncentrosymmetric oxide interfaces. *Nat. Commun.* **10**, 4510 (2019).
23. Vaz, D. C. et al. Determining the Rashba parameter from the bilinear magnetoresistance response in a two-dimensional electron gas. *Phys. Rev. Mater.* **4**, 071001 (2020).
24. Zhang, J. E. et al. Anisotropic bilinear magnetoresistance in (110) SrTiO<sub>3</sub>-based two-dimensional electron gas. *Phys. Rev. B* **104**, 045114 (2021).
25. Lu, X. F. et al. Nonlinear transport and radio frequency rectification in BiTeBr at room temperature. *Nat. Commun.* **15**, 245 (2024).
26. Kocsis, M. et al. In-situ tuning of symmetry-breaking-induced nonreciprocity in the giant-Rashba semiconductor BiTeBr. *Phys. Rev. Res.* **3**, 033253 (2021).
27. Disa, A. S., Nova, T. F. & Cavalleri, A. Engineering crystal structures with light. *Nat. Phys.* **17**, 1087-1092 (2021).
28. Suda, M., Kato, R. & Yamamoto, H. M. Light-induced superconductivity using a photoactive electric double layer. *Science* **347**, 743-746 (2015).
29. Liu, R. X. et al. Light-induced Mott-insulator-to-metal phase transition in ultrathin intermediate-spin ferromagnetic perovskite ruthenates. *Adv. Mater.* **35**, 2211612 (2023).
30. Niu, W. et al. Fully optical modulation of the two-dimensional electron gas at the  $\gamma$ -Al<sub>2</sub>O<sub>3</sub>/SrTiO<sub>3</sub> interface. *J. Phys. Chem. Lett.* **13**, 2976-2985 (2022).
31. Liu, C. J. et al. Two-dimensional superconductivity and anisotropic transport at KTaO<sub>3</sub> (111) interfaces. *Science* **371**, 716-721 (2021).
32. Chen, Z. et al. Electric field control of superconductivity at the LaAlO<sub>3</sub>/KTaO<sub>3</sub> (111) interface. *Science* **372**, 721-724 (2021).
33. Arnault, E. G. et al. Anisotropic superconductivity at KTaO<sub>3</sub>(111) interfaces. *Sci. Adv.* **9**, eadf1414 (2023).
34. Zhang, G. Q. et al. Spontaneous rotational symmetry breaking in KTaO<sub>3</sub> heterointerface superconductors. *Nat. Commun.* **14**, 3046 (2023).
35. Zhang, H. et al. Unusual electric and optical tuning of KTaO<sub>3</sub>-based two-dimensional electron gases with 5d orbitals. *ACS Nano* **13**, 609-615 (2019).
36. Liu, J. et al. Confinement-enhanced Rashba spin-orbit coupling at the LaAlO<sub>3</sub>/KTaO<sub>3</sub> interface via LaAlO<sub>3</sub> thickness control. *Phys. Status Solidi RRL* **17**, 2200441 (2023).

37. Zhang, C. et al. Ion-liquid-gated KTaO<sub>3</sub>-based electric double layer transistor. *IEEE Electron Device Lett.* **44**, 1987-1990 (2023).
38. Varotto, S. et al. Direct visualization of Rashba-split bands and spin/orbital-charge interconversion at KTaO<sub>3</sub> interfaces. *Nat. Commun.* **13**, 6165 (2022).
39. Gan, Y. L. et al. Light-induced giant Rashba spin-orbit coupling at superconducting KTaO<sub>3</sub>(110) heterointerfaces. *Adv. Mater.* **35**, 2300582 (2023).
40. Zhang, H. R. et al. High-mobility spin-polarized two-dimensional electron gases at EuO/KTaO<sub>3</sub> interfaces. *Phys. Rev. Lett.* **121**, 116803 (2018).
41. Ren, T. S. et al. Two-dimensional superconductivity at the surfaces of KTaO<sub>3</sub> gated with ionic liquid. *Sci. Adv.* **8**, eabn4273 (2022).
42. Goyal, S., Wadehra, N. & Chakraverty, S. Tuning the electrical state of 2DEG at LaVO<sub>3</sub>-KTaO<sub>3</sub> interface: Effect of light and electrostatic gate. *Adv. Mater. Interfaces* **7**, 2000646 (2020).
43. Qi, S. J. et al. Large optical tunability of 5d 2D electron gas at the spinel/perovskite  $\gamma$ -Al<sub>2</sub>O<sub>3</sub>/KTaO<sub>3</sub> heterointerface. *Adv. Mater. Interfaces* **9**, 2200103 (2022).
44. Chen, Z. et al. Two-dimensional superconductivity at the LaAlO<sub>3</sub>/KTaO<sub>3</sub>(110) heterointerface. *Phys. Rev. Lett.* **126**, 026802 (2021).
45. Liu, Y. et al. Superconductivity in epitaxially grown LaVO<sub>3</sub>/KTaO<sub>3</sub> (111) heterostructures. *Chin. Phys. B* **32**, 037305 (2023).
46. Liang, H. X. et al. Nonmonotonically tunable Rashba spin-orbit coupling by multiple-band filling control in SrTiO<sub>3</sub>-based interfacial d-electron gases. *Phys. Rev. B* **92**, 075309 (2015).
47. Shibuya, K. et al. Observation of SrTiO<sub>3</sub> in-gap states by depletion mode field effect. *Appl. Phys. Lett.* **92**, 032109 (2008).
48. Zeng, S. W. et al. Oxygen electromigration and energy band reconstruction induced by electrolyte field effect at oxide interfaces. *Phys. Rev. Lett.* **121**, 146802 (2018).
49. Hua, X. Y. et al. Tunable two-dimensional superconductivity and spin-orbit coupling at the EuO/KTaO<sub>3</sub>(110) interface. *npj Quantum Mater.* **7**, 97 (2022).
50. Cheng, L. et al. Optical Manipulation of Rashba Spin-Orbit Coupling at SrTiO<sub>3</sub>-Based Oxide Interfaces. *Nano Lett.* **17**, 6534-6539 (2017).
51. Wadehra, N. et al. Electronic structure modification of the KTaO<sub>3</sub> single-crystal surface by Ar<sup>+</sup> bombardment. *Phys. Rev. B* **96**, 115423 (2017).
52. Lee, J. H. et al. Nonreciprocal transport in a Rashba ferromagnet, delafossite PdCoO<sub>2</sub>. *Nano Lett.* **21**, 8687-8692 (2021).
53. Legg, H. F. et al. Giant magnetochiral anisotropy from quantum-confined surface states of topological insulator nanowires. *Nat. Nanotechnol.* **17**, 696-700 (2022).
54. Wang, Y. et al. Large bilinear magnetoresistance from Rashba spin-splitting on the surface of a topological insulator. *Phys. Rev. B* **106**, L241401 (2022).



55. Yasuda, K. et al. Nonreciprocal charge transport at topological insulator/superconductor interface. *Nat. Commun.* **10**, 2734 (2019).
56. Maniv, E. et al. Strong correlations elucidate the electronic structure and phase diagram of LaAlO<sub>3</sub>/SrTiO<sub>3</sub> interface. *Nat. Commun.* **6**, 8239 (2015).
57. Lesne, E. et al. Designing spin and orbital sources of Berry curvature at oxide interfaces. *Nat. Mater.* **22**, 576-582 (2023).
58. Maekawa, S. & Fukuyama, H. Magnetoresistance in two-dimensional disordered systems: effects of Zeeman splitting and spin-orbit scattering. *J. Phys. Soc. Jpn* **50**, 2516-2524 (1981).
59. Cavaglia, A. D. et al. Tunable Rashba spin-orbit interaction at oxide interfaces. *Phys. Rev. Lett.* **104**, 126803 (2010).
60. Bareille, C. et al. Two-dimensional electron gas with six-fold symmetry at the (111) surface of KTaO<sub>3</sub>. *Sci. Rep.* **4**, 3586 (2014).
61. Kresse, G. & Furthmuller, J. Efficient iterative schemes for ab initio total-energy calculations using a plane-wave basis set. *Phys. Rev. B* **54**, 11169-11186 (1996).
62. Kresse, G. & Joubert, D. From ultrasoft pseudopotentials to the projector augmented-wave method. *Phys. Rev. B* **59**, 1758-1775 (1999).
63. Zhang, Y. K. & Yang, W. T. Comment on "Generalized gradient approximation made simple". *Phys. Rev. Lett.* **80**, 890 (1998).
64. Blochl, P. E. Projector augmented-wave method. *Phys. Rev. B* **50**, 17953 (1994).
65. Marzari, N. & Vanderbilt, D. Maximally localized generalized Wannier functions for composite energy bands. *Phys. Rev. B* **56**, 12847-12865 (1997).
66. Souza, I., Marzari, N. & Vanderbilt, D. Maximally localized Wannier functions for entangled energy bands. *Phys. Rev. B* **65**, 035109 (2002).
67. Pizzi, G. et al. Wannier90 as a community code: New features and applications. *J. Phys. Condens. Matter* **32**, 165902 (2020).

## Supplementary Information

### Light-induced giant enhancement of nonreciprocal transport at $\text{KTaO}_3$ -based interfaces

Xu Zhang<sup>1,†</sup>, Tongshuai Zhu<sup>2,3,†</sup>, Shuai Zhang<sup>2,†</sup>, Zhongqiang Chen<sup>1</sup>, Anke Song<sup>1</sup>,  
Chong Zhang<sup>1</sup>, Rongzheng Gao<sup>1</sup>, Wei Niu<sup>1</sup>, Yequan Chen<sup>1</sup>, Fucong Fei<sup>2</sup>, Yilin Tai<sup>4</sup>,  
Guoan Li<sup>5</sup>, Binghui Ge<sup>4</sup>, Wenkai Lou<sup>6</sup>, Jie Shen<sup>5</sup>, Haijun Zhang<sup>2</sup>, Kai Chang<sup>6</sup>,  
Fengqi Song<sup>2,\*</sup>, Rong Zhang<sup>1,7,\*</sup> & Xuefeng Wang<sup>1,\*</sup>

\*E-mail: songfengqi@nju.edu.cn; rzhang@nju.edu.cn; xfwang@nju.edu.cn

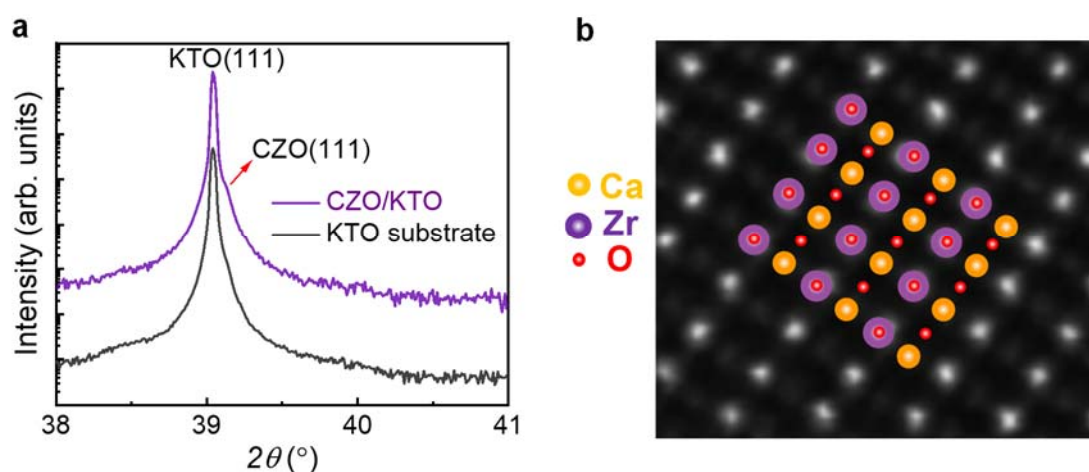
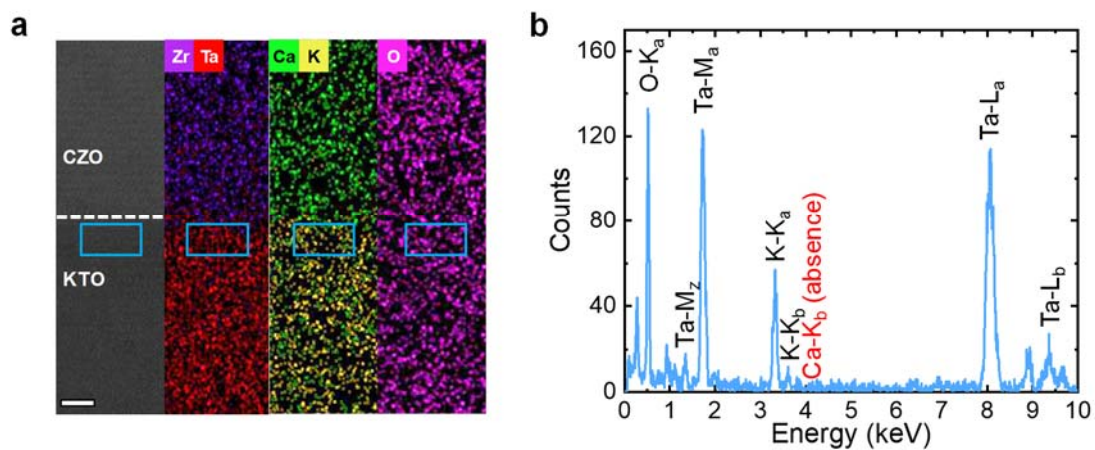
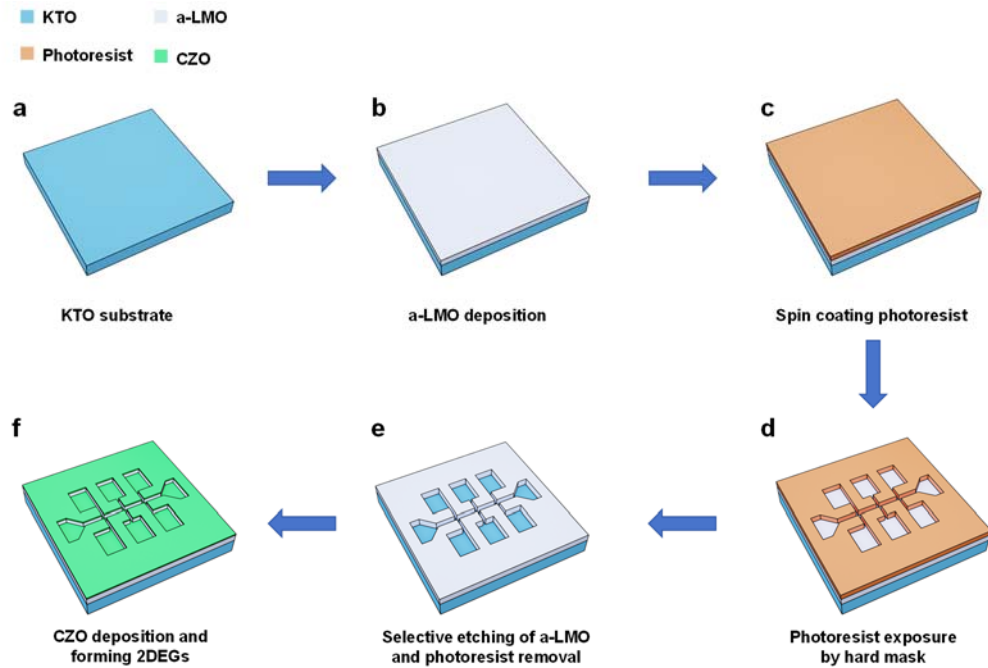


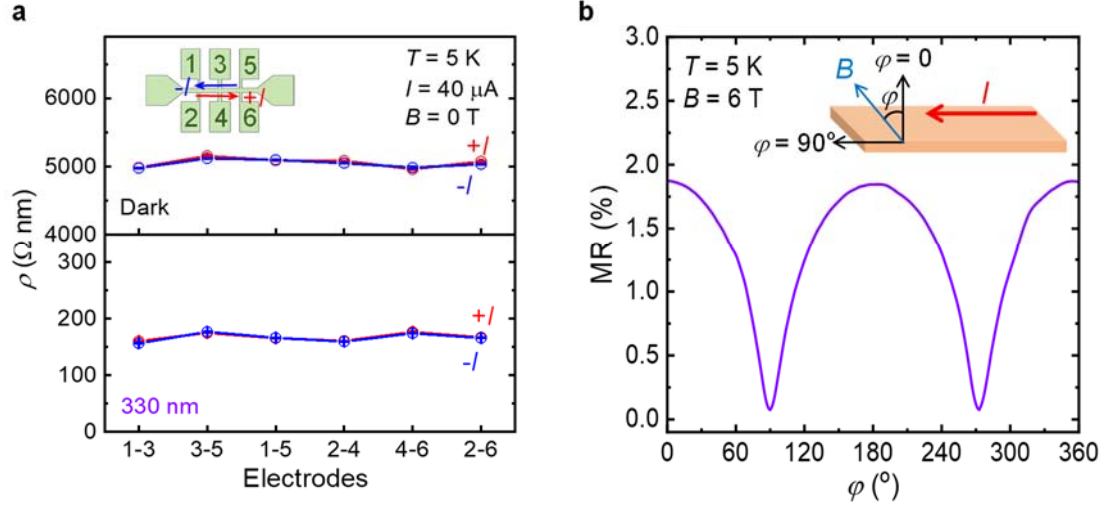
**Fig. S1. Basic structural characterization.** **a**,  $\theta$ - $2\theta$  x-ray diffraction (XRD) pattern for the CZO/KTO (111) sample. The diffraction peak of CZO can be traced from the KTO substrate, implying the excellent epitaxy. **b**, The enlarged atomic configuration overlapping on the STEM image, which is taken from **Fig. 1b**.



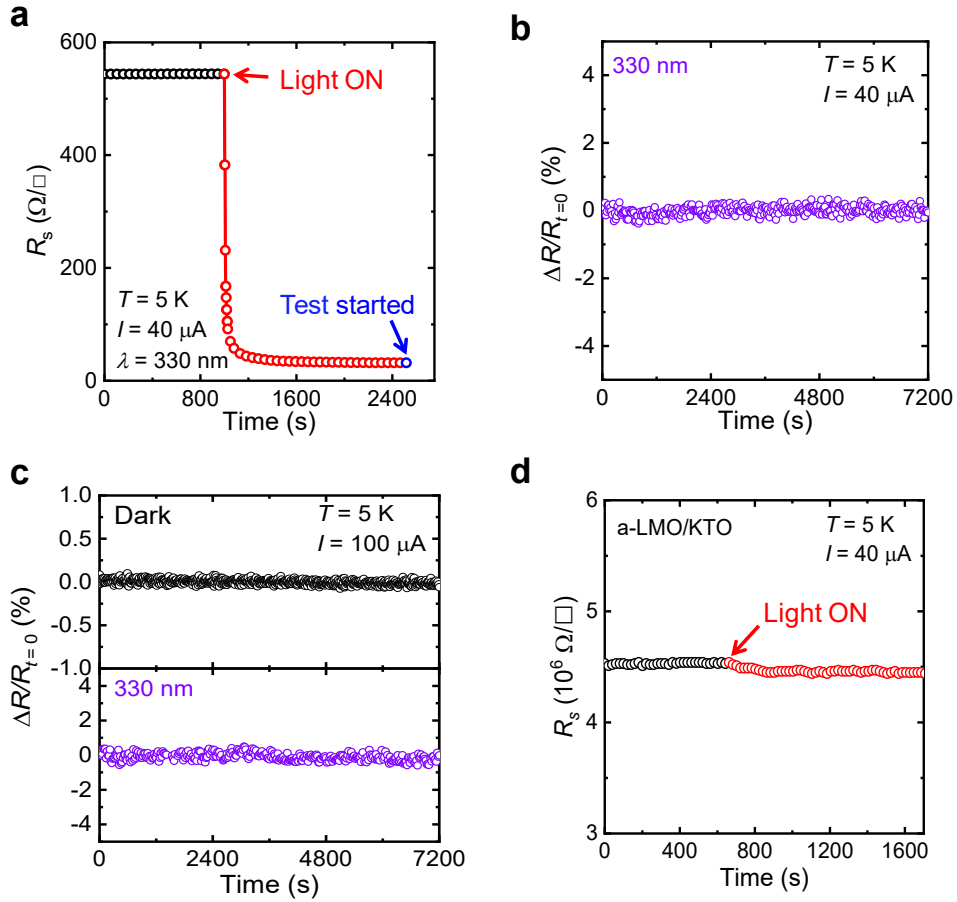
**Supplementary Fig. 2. EDX elemental mapping and the corresponding spectrum.** **a**, EDX elemental mapping at the interface. A quantitative spectroscopic analysis is conducted in the region within the blue boxed area. The white dashed line is a guide to indicate the interface. The scale bar is 5 nm. **b**, The corresponding EDX spectrum, where the characteristic peaks of K, Ta and O elements are clearly seen. However, no peaks of Ca element are detected, indicating the noticeable Ca element in the KTO substrate in **a** is actually an artifact due to the very close energy edges of Ca and K from EDX.



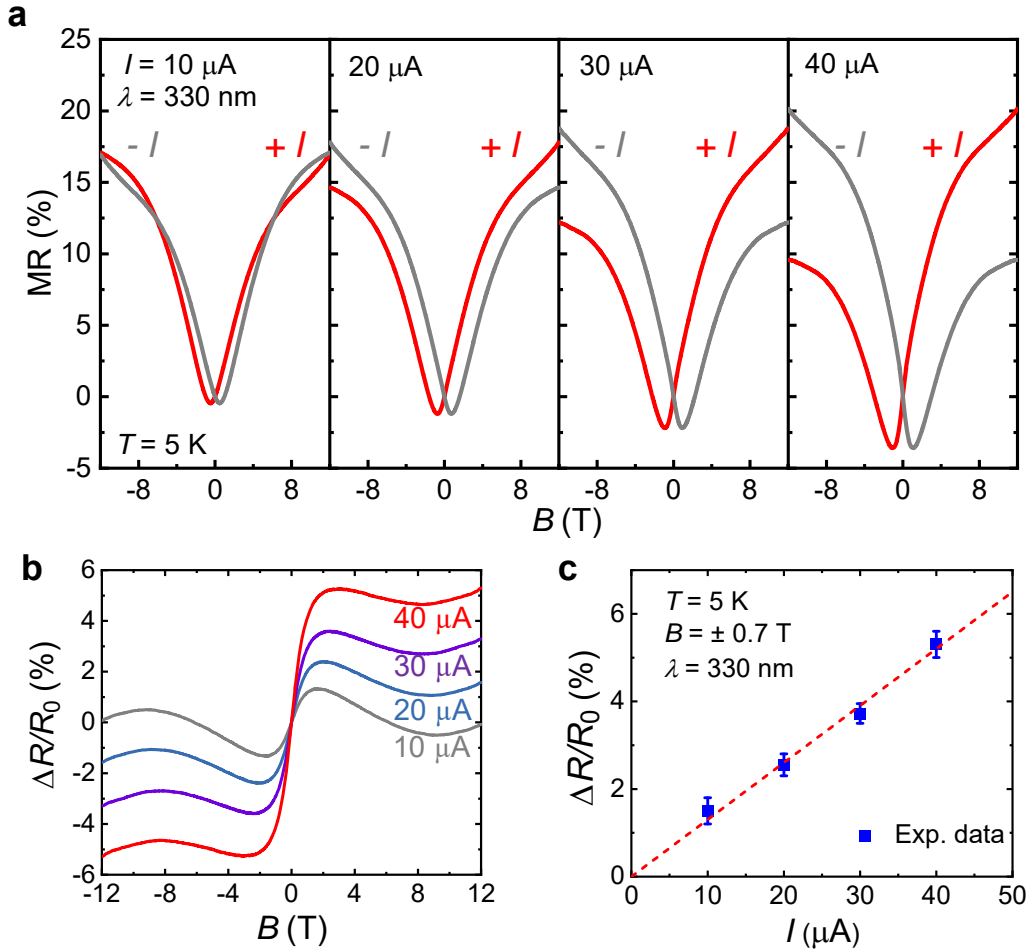
**Supplementary Fig. 3. Schematic illustration of the Hall-bar device fabrication process.** **a-b**, The amorphous  $\text{LaMnO}_3$  (a-LMO) film is deposited by the PLD on the KTO substrate. **c**, The photoresist is spin-coated onto the a-LMO surface. **d**, Hall-bar pattern of photoresist is fabricated by the ultraviolet exposure. **e**, The selective etching by HCl/KI solution and the removal of the rest photoresist, forming the Hall-bar pattern of the a-LMO film. **f**, The CZO layer is deposited by PLD. The 2DEGs thus forms at the a-LMO-patterned CZO/KTO interfaces.



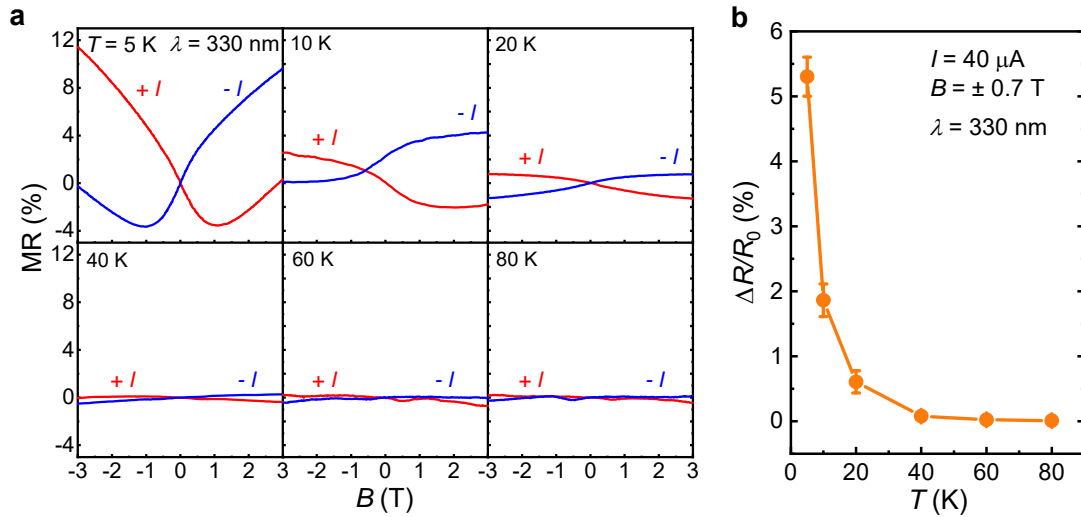
**Supplementary Fig. 4. Homogeneity test and the 2D conducting characteristic of the 2DEGs at the CZO/KTO interfaces.** **a**, The resistivity of the arbitrarily selected electrodes by applying both  $I = \pm 40 \mu\text{A}$  in the dark and under 330-nm illumination, respectively. The temperature is 5 K without the applied external field. The inset is the sketch of this Hall-bar electrodes for the homogeneity test. It can be seen that there is no significant difference of the resistivity between each electrode in both dark condition and under illumination, indicating the excellent homogeneity of the conducting channel of 2DEGs. Besides, no remarkable difference is observed when applying the opposite-direction current, further ruling out the inhomogeneity of the carrier distribution. The lines are drawn as guides for the eyes. **b**, The anisotropic MR as a function of the direction of the applied field at 5 K and 6 T for the CZO/KTO heterostructures. The inset shows the sketch of the anisotropic MR measurement. The sharp peaks at  $90^\circ$  and  $270^\circ$  when the field is applied parallel or antiparallel to the current indicate the 2D conduction characteristic and also the uniformity of the 2DEGs at the interface. The thickness of the conduction layer ( $t$ ) can be estimated by adopting the formula of  $t = h/(e^2 k_F R_s \sqrt{\alpha})$ , where  $h$  is the Planck constant,  $e$  is the electron charge,  $k_F$  is the Fermi wave vector ( $k_F = \sqrt{2\pi n_s}$ ),  $R_s$  is the sheet resistance, and  $\alpha$  is defined by the ratio of the perpendicular MR to the parallel MR. The conduction layer thickness of KTO-based 2DEGs is thus estimated to be  $\sim 4.35$  nm.



**Supplementary Fig. 5. Stability test of the 2DEGs at the CZO/KTO interfaces.** **a**, The time evolution of the sheet resistance under the in-situ light illumination at 330 nm at 5 K. The MR and Hall effect measurements were carried out when the sheet resistance is stabilized under the light illumination. **b**, The time evolution of the ratio of the resistance change ( $\Delta R/R_{t=0}$ ) under 330-nm illumination at 5 K.  $R_{t=0}$  represents the initial sheet resistance at  $t = 0$ .  $\Delta R = R_t - R_{t=0}$  represents the resistance change. The applied current is 40 μA. A negligible resistance variation of less than 0.5% is observed with the time evolution for at least 2 h, excluding the light-induced heating effect. **c**, The time evolution of  $\Delta R/R_{t=0}$  in the dark and under 330-nm illumination at 5 K, respectively. The applied current is as large as 100 μA. The resistance still maintains nearly unchanged (within 0.6%) even under 330-nm illumination at 5 K for at least 2 h, ruling out any light-induced/large-current-induced heating effect during the light-irradiation measurements. **d**, The time evolution of the resistance at the a-LMO/KTO interface under the light illumination at 330 nm at 5 K. It is seen that the a-LMO/KTO interface always maintains insulating ( $\sim 10^6$  Ω/□) during the illumination.

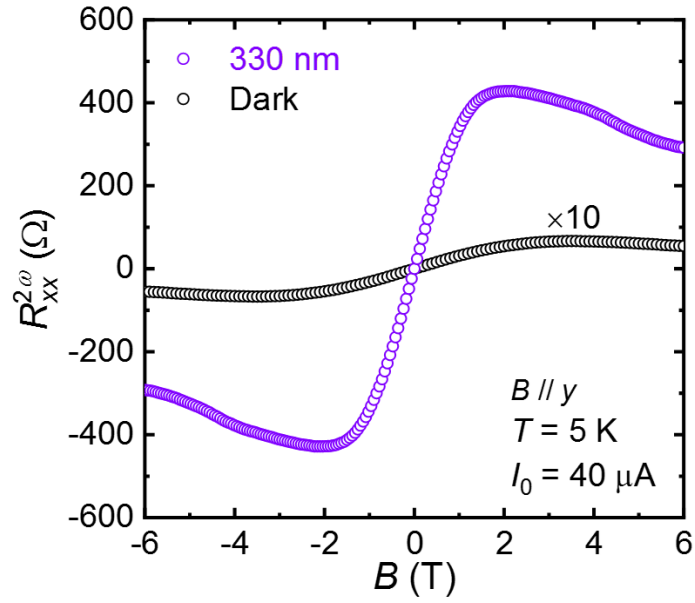


**Supplementary Fig. 6. Current dependence of the nonreciprocal transport.** **a**, In-plane MR curves measured at 330 nm with applied different currents at 5 K. **b**, The ratio of the resistance change ( $\Delta R/R_0$  extracted from **a**) as a function of magnetic field at various currents. **c**,  $\Delta R/R_0$  at  $\pm 0.7$  T as a function of applied current. The red dashed line is a guide to the eye, indicating the linear behavior. The error bars indicate the uncertainty from the experimental results. The red dashed line is the linear fitting.

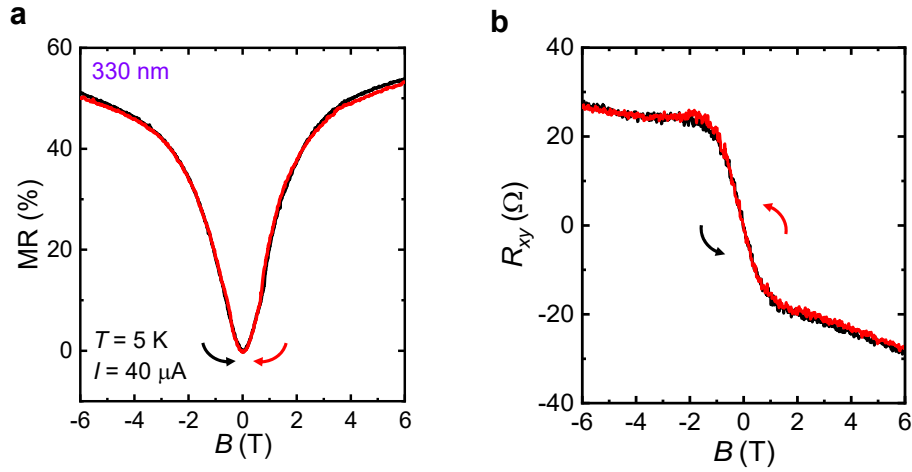


**Supplementary Fig. 7. Temperature dependence of the nonreciprocal transport. a,** In-plane MR curves measured at 330 nm under different temperatures. The applied current  $I = \pm 40 \mu\text{A}$ . **b,** The ratio of the resistance change ( $\Delta R/R_0$  at  $\pm 0.7 \text{ T}$  extracted from **a**) as a function of temperature. The nonreciprocal transport vanishes above 40 K, which is attributed to the disruption of spin-momentum locking by quantum fluctuations at relatively high temperatures. The error bars indicate the uncertainty from the experimental results. The line connecting the data points is drawn as a guide for the eyes.

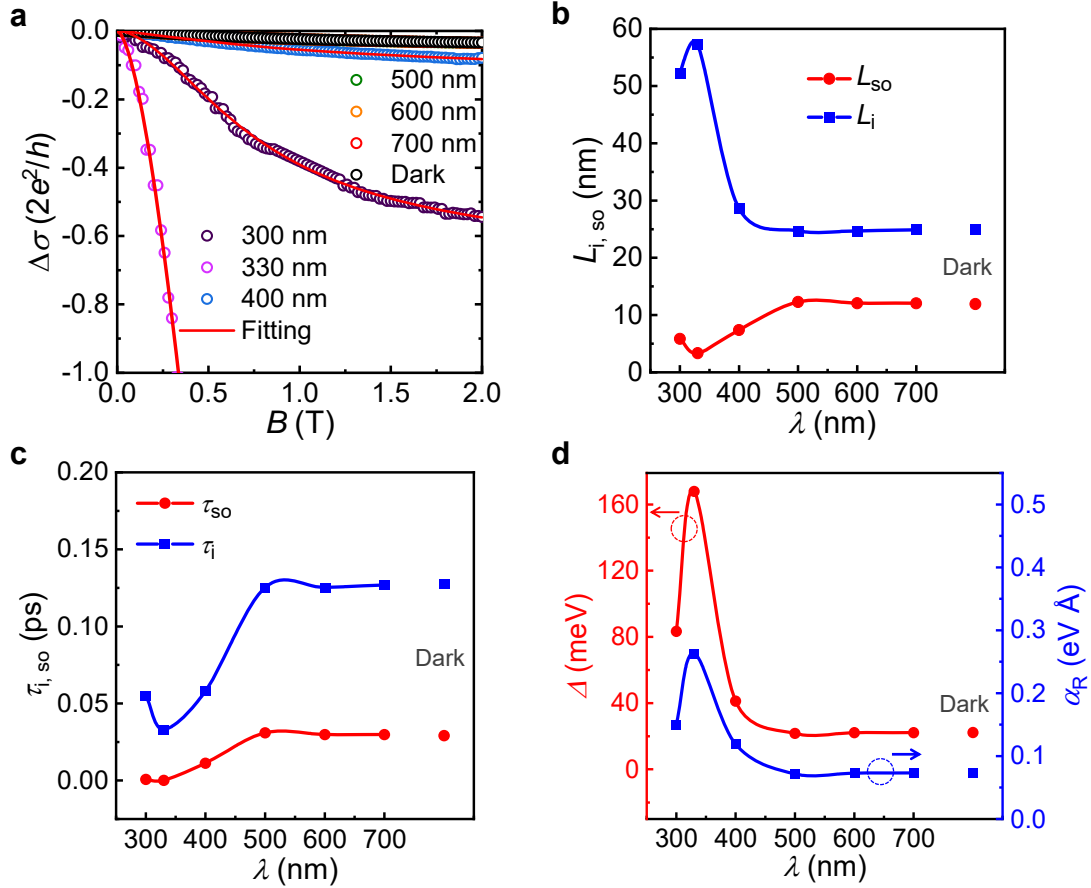




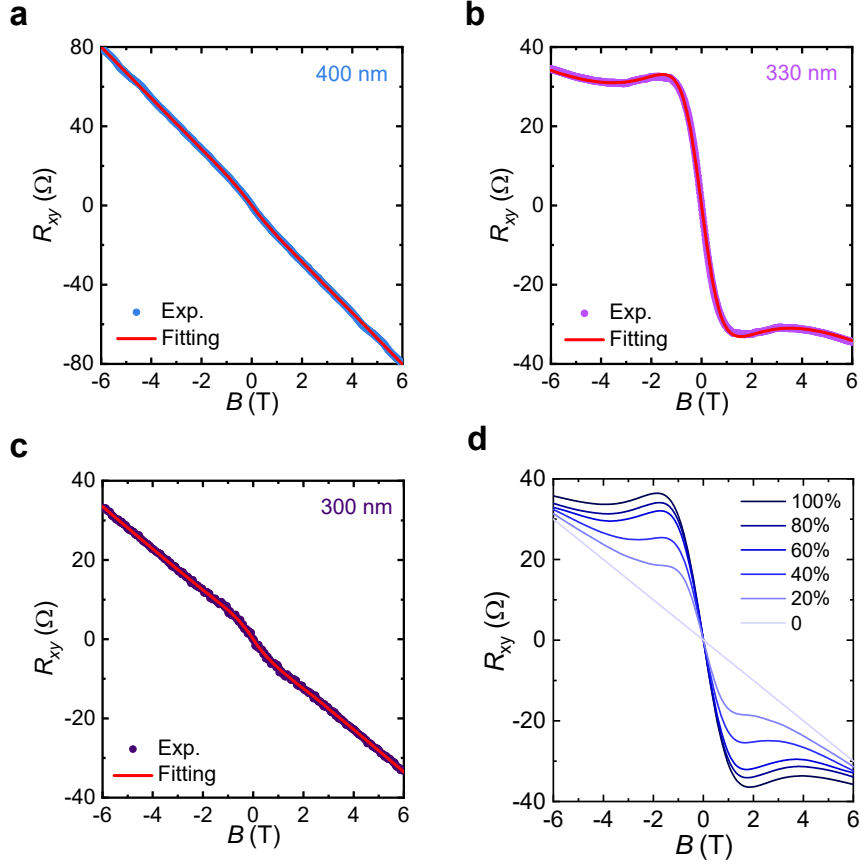
**Supplementary Fig. 8. Second harmonic measurements for the nonreciprocal transport of KTO-based 2DEGs.** The second-harmonic resistance ( $R_{xx}^{2\omega}$ ) as a function of in-plane magnetic field under 330-nm illumination and in the dark at 5 K. The nonreciprocal transport coefficient under 330-nm illumination also has the giant enhancement of three orders of magnitude, which further confirms the light-induced giant enhancement of nonreciprocal transport at the CZO/KTO interface.



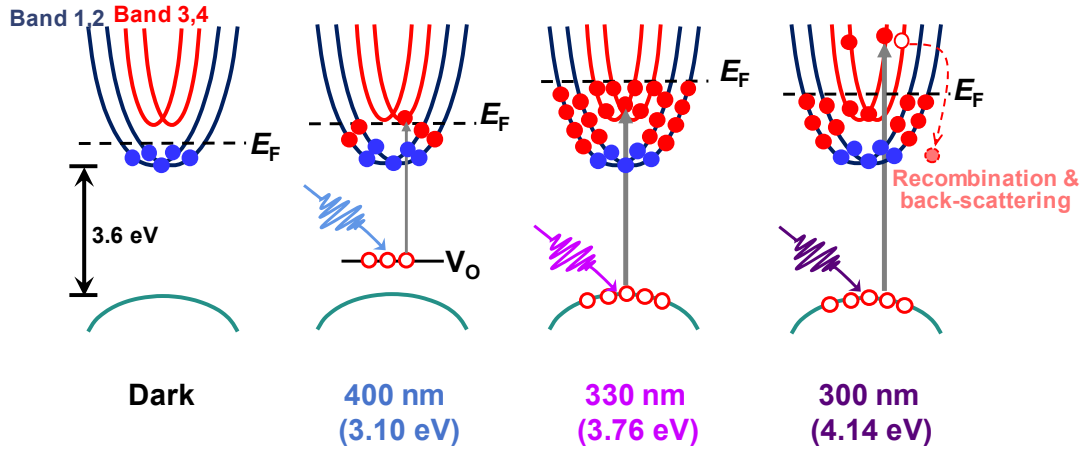
**Supplementary Fig. 9. Hysteretic MR and  $R_{xy}$  measurements.** **a,b**, MR and Hall curves under 330-nm irradiation with the applied out-of-plane magnetic field swept back and forth. We cannot observe any discernible hysteresis in both MR and Hall curves, indicating that light irradiation in our experiments cannot induce any ferromagnetic/spin-polarized 2DEGs at CZO/KTO interfaces.



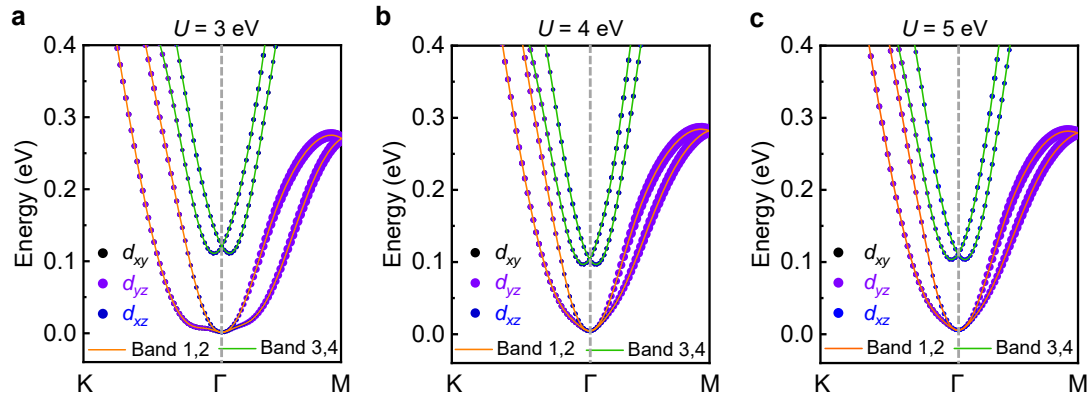
**Supplementary Fig. 10. The magnetoconductance curves and the deduced other SOC-related parameters at various wavelengths at 5 K. a**, The fitting curves of  $\Delta\sigma$  according to the MF model at various wavelengths. This is the enlarged figure of **Fig. 3b**. **b-d**, The wavelength-dependent spin relaxation length ( $L_{so}$ ) and dephasing length ( $L_i$ ) in **b**, spin relaxation time ( $\tau_{so}$ ) and inelastic scattering time ( $\tau_i$ ) in **c**, and spin-splitting energy ( $\Delta$ ) and Rashba coefficient ( $\alpha_R$ ) in **d**, respectively. The corresponding parameters of the dark condition are also included in **b-d** for comparison.



**Supplementary Fig. 11. Hall curves perfectly fitted using the two-band model.** **a-c**, The fitting curves of the Hall resistance at 400-nm, 330-nm and 300-nm illumination using the two-band model (equations (3) and (4) in the main text). Note that the kinks occurring at the Hall resistance at around  $\pm 1$  T of 330-nm illumination in **b** are originated from the significant excitation of the second type of carriers with extremely high mobility at 330 nm. **d**, The Hall curves measured at various light powers normalized with that in **b**, indicating the clear excitation process from single type carrier (linear Hall resistance) to two types of carriers (nonlinear Hall resistance) with increasing light power.



**Supplementary Fig. 12. The physical mechanism of photocarrier excitation.** In the dark, 2DEGs form at the CZO/KTO interface and there are abundant electrons in the potential well, as shown in Fig. 2c. Under the 400-nm illumination, electrons are excited from in-gap states of KTO to the CBM and transfer to the potential well. In this case, the intrinsic carriers increase a little and the second-type carriers emerge (grey arrows). Under the excitation of 330-nm light, abundant electrons are excited from the VBM to the CBM, inducing the considerable increase of both the intrinsic carriers and the second-type carriers as well as the  $E_F$ -level upward shift. However, under the excitation of 300-nm light, the total carrier density cannot be increased further. In this case, electrons can be excited to the higher subbands (above Band 3,4) of the  $t_{2g}$  conduction band. The higher-energy photoelectrons lead to increased interactions between electrons and the lattice (phonons), which results in a longer time for the electrons to return to a lower energy state. During this enhanced relaxation process, more photogenerated electrons would experience a notable competition between the weak localization and weak antilocalization in addition to the likely recombination of photogenerated electrons and holes. Hence, compared to the condition under 330-nm illumination, the final carrier density responsible for conductivity decreases and  $E_F$  level moves downward.



**Supplementary Fig. 13. The band structures from first-principles calculations plus Hubbard  $U$ .** a-c, The calculated electronic band structures (Band 1-4, orange and green lines) and the weight of  $d_{xy}$ ,  $d_{yz}$  and  $d_{xz}$  (black, purple and blue circles) orbitals of 12-Ta layers of KTO (111) surface for  $U = 3, 4$  and  $5$  eV, respectively. The weight of the orbitals is expressed by the size of the corresponding circles. There is no significant difference among calculated electronic band structures of KTO under different Hubbard  $U$  values, indicating that light only impacts on the location of  $E_F$ , thereby influencing the Rashba SOC strength as well as the nonreciprocal transport.